Available online at www.sciencedirect.com
ScienceDirect
International Journal of Heat and Mass Transfer 51 (2008) 3144–3152
International Journal of HEAT and MASS TRANSFER
www.elsevier.com/locate/ijhmt

# Heat-transfer distribution for an impinging laminar flame jet to a flat plate

M.J. Remie [a], G. Särner [b], M.F.G. Cremers [a], A. Omrane [b], K.R.A.M. Schreel [a], L.E.M. Aldén [b], L.P.H. de Goey [a,*]

[a] Eindhoven University of Technology, Department of Mechanical Engineering, P.O. Box 513, 5600 MB Eindhoven, The Netherlands
[b] Lund Institute of Technology, Division of Combustion Physics, P.O. Box 118, SE-221 00 Lund, Sweden

Received 14 May 2007; received in revised form 13 August 2007
Available online 4 December 2007

**Abstract**

Impinging flame jets are widely used in applications where high heat-transfer rates are needed, for instance in the glass industry. During the heating process of glass products, internal thermal stresses develop in the material due to temperature gradients. In order to avoid excessive thermal gradients as well as overheating of the hot spots, it is important to know and control the temperature distribution inside a heated glass product. Therefore, it is advantageous to know the relation describing the convective heat–flux distribution at the heated side of a glass product. In a previous work, we presented a heat–flux relation applicable for the hot spot of the target [M.J. Remie, G. Särner, M.F.G. Cremers, A. Omrane, K.R.A.M. Schreel, M. Aldén, L.P.H. de Goey, Extended heat-transfer relation for an impinging laminar flame jet to a flat plate, Int. J. Heat Mass Transfer, in press]. In this paper, we present an extension of this relation, which is applicable for larger radial distances from the hot spot.


*Keywords:* Impinging flame jet; Heat-transfer; Oxy-fuel; Phosphorescence

## 1. Introduction

Impinging laminar flame jets are often used to improve the heat-transfer to a surface. Applications can for instance be found in the glass industry. Glass products are melted, cut, formed, annealed, softened and shaped using flame jets in many aspects of the glass fabrication processes. It is well reckoned that these jets yield very high heat-transfer coefficients [1–4]. Examples of experiments quantifying the heat-transfer characteristics of impinging flame jets can be found in references [5–11].

The main heat-transfer mechanism for impinging flame jets is forced convection. Radiation from the flame is negligible because of the very low emissivity of a hot gas layer of small thickness [1,12,13]. Often the burners are supplied with a pure fuel and oxygen mixture to enhance the heat-transfer. When the convective heat flux has to be determined, these flames can be treated as hot inert jets. This approach is plausible because the flow behavior of flame jets and hot isothermal jets is comparable [1,12]. The main difference between the oxy-fuel flames and the hot inert jets is that the flames contain a lot of free radicals as a result of dissociation of stable molecules like $H_2O$ and $CO_2$ at high temperatures. These free radicals recombine in the cold boundary layer releasing extra heat, a mechanism often indicated as thermochemical heat release (TCHR). A correction which takes these chemical reactions and the resulting extra heat input into account has to be performed afterwards to obtain the total heat transfer.

When the heat-transfer of inert jets needs to be estimated, it is very useful from an engineering point of view to have simple analytical expressions for this heat-transfer at one's disposal. In previous publications [14,15], we presented an analytical relation to calculate the heat-transfer from stoichiometric laminar impinging flame jets to the

* Corresponding author. Fax: +31 40 2433445.
*E-mail address:* l.p.h.d.goey@tue.nl (L.P.H. de Goey).

0017-9310/$ - see front matter © 2007 Elsevier Ltd. All rights reserved.
doi:10.1016/j.ijheatmasstransfer.2007.08.036

**Nomenclature**

| | |
|---|---|
| $a$ | applied strain rate (1/s) |
| $c_p$ | specific heat at constant pressure (J/(kg K)) |
| $H$ | flame tip-to-plate distance (m) |
| $H^*$ | critical distance (m) |
| $H_{\text{flame}}$ | flame height (m) |
| $H_{\text{tot}}$ | burner-to-plate distance (m) |
| $h$ | heat-transfer coefficient (W/(m$^2$ K)) |
| $K$ | strain rate of the burnt gases (1/s) |
| $L$ | thickness of the glass plate (m) |
| $Nu$ | Nusselt number (–) |
| $Pe$ | Peclet number (–) |
| $Pr$ | Prandtl number (–) |
| $q$ | heat flux (W/m$^2$) |
| $R$ | burnt gas jet radius (m) |
| $Re$ | Reynolds number (–) |
| $T$ | temperature (K) |
| TCHR | TCHR factor (–) |
| $t$ | time (s) |
| $U$ | uniform flow velocity (m/s) |
| $u$, $v$ | velocity components (m/s) |
| $x_\delta$ | viscous boundary layer thickness (m) |
| $x$, $r$ | cylindrical coordinates (m) |

*Greek symbols*

| | |
|---|---|
| $\alpha$ | thermal diffusivity (m$^2$/s) |
| $\beta$ | velocity gradient (1/s) |
| $\lambda$ | thermal conductivity (W/(m K)) |
| $\mu$ | dynamic viscosity (kg/(m s)) |
| $\nu$ | kinematic viscosity (m$^2$/s) |
| $\rho$ | density (kg/m$^3$) |

*Abbreviations*

| | |
|---|---|
| CFD | computational fluid dynamics |
| ICCD | intensified charge-coupled device |
| MFC | mass flow controller |
| TCHR | thermochemical heat release |

hot spot on a target. Validation of this expression has been performed successfully by comparing it to the semi-analytical relation derived by Sibulkin [16], which has been the basis of most other experimental and theoretical results for the laminar heat transfer of an impinging flow to a body of revolution [17–21]. Furthermore, experimental validation using phosphor thermometry measurements has been presented as well [15].

In this paper, we will present an extension of the above mentioned heat-transfer relation for stoichiometric flame jets. With this extension, not only the heat-transfer to the hot spot of the target can be calculated, but the complete heat-transfer distribution to a flat target can be predicted as well. To that purpose, in the following section we will start by reviewing shortly how the analytical relation for the convective heat flux to the hot spot was derived. For an extensive derivation, the reader is referred to our previous publication [15]. Subsequently, the extension of the derived relation will be treated, in order to be able to calculate the heat-transfer distribution close to the hot spot. Finally, we will present results of temperature measurements of a quartz plate which was heated by a methane-oxygen as well as a hydrogen–oxygen flame, carried out to validate the analytically and numerically obtained heat-transfer distribution expressions.

## 2. Analytical solution for the heat-transfer

Fig. 1 shows a generalized picture of a single circular premixed flame jet impinging normal to a flat surface. Four characteristic regions can be distinguished in the flow structure: the flame jet region, the free jet region, the stagnation flow region and the impingement surface. Cremers et al.

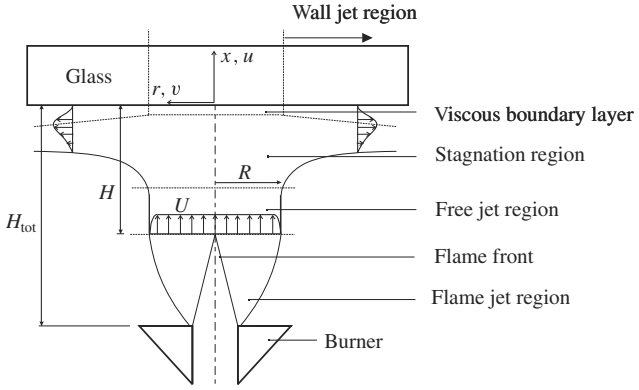


Fig. 1. Schematic overview of a stagnation flame impinging to a plane surface.

[22] have shown that the typical time scales of the regions are different. Consequently, the regions can be decoupled, treated and solved separately and coupled again afterwards. If the plate is placed close to the flame, the flame front and the stagnation boundary layer will interact and decoupling of the regions is not allowed anymore; the resulting error of the predicted heat flux, however, is only 10% at most [23]. In order to derive the relation for the heat flux to the hot spot of the plate, which has a width of $2R$, we will focus on the free jet region and the stagnation region. In previous work [24], we have shown that for a flame where pure oxygen is supplied to the oxidizer stream, the burnt gases form a flow profile very close to a plug flow after the flame front. At the edges of the stream tube, the velocity of the burnt gases rapidly drops. Input parameters for the model will be the resulting plug flow velocity $U$ (m/

s) and plug flow jet radius $R$ (m), which can be calculated using the unburnt gas parameters [24], as well as the distance from the flame front to the plate $H$ (m).

In [14,15], we have shown that if we have no free jet region, so if the plate is positioned close to the flame tip, $H \leqslant R$, the solution for the heat-transfer from the burnt gases to the plate $q_0$ (W/m$^2$) is given by

$$q_0 = \lambda \left.\frac{\mathrm{d}T}{\mathrm{d}x}\right|_0 = \frac{\lambda(T_0 - T_{\mathrm{flame}})}{\int_{-H}^{0} \exp\left[-\frac{1}{\alpha}\int_s^0 u\,\mathrm{d}x\right]\mathrm{d}s}, \tag{1}$$

with $\lambda$ the conductivity coefficient (W/(m K)), $T$ the temperature (K), $\alpha = \lambda/(\rho c_p)$ the thermal diffusivity (m$^2$/s), $\rho$ the density (kg/m$^3$), $c_p$ the heat capacity of the burnt gas flow (J/(kg K)) and $u$ the velocity of the burnt gases (m/s). By decoupling the domain in a region consisting of the viscous boundary layer, $-x_\delta < x < 0$, and a region far from the plate to the viscous boundary layer, $-H < x < -x_\delta$, two relations for the velocity profiles were found which could be linked at $x = -x_\delta$ [15]:

$$u_1(x) = a x_\delta \left(\frac{x^3}{3x_\delta^3} + \frac{x^2}{x_\delta^2}\right) \quad \text{for } -x_\delta < x < 0, \tag{2}$$

$$u_2(x) = -\frac{a^2}{4U}(x + x_\delta/3)^2 - a(x + x_\delta/3) \quad \text{for } -H < x < -x_\delta, \tag{3}$$

respectively, with $x_\delta = 2\sqrt{\nu/a}$ the thickness of the boundary layer (m), $a = 2U/H$ the maximum strain rate (1/s), $\nu = \mu/\rho_b$ the kinematic viscosity (m$^2$/s) and $\mu$ the dynamic viscosity (kg/(m s)). Implementing the velocity relations $u_1$ (2) and $u_2$ (3) in the relation describing the heat flux (1) results in a relation for the heat flux, which can be found in Ref. [15].

Numerical validation of this relation describing the convective heat transfer of an impinging flame to the hot spot of a flat object for $H \leqslant R$ was performed using Fluent [25]. Using Fluent, it is also possible to extend this relation for $H > R$. It was observed that the maximum strain rate $a = K_{\max}$ just before the plate determines the heat flux [15]. For small flame tip-to-plate distances, the maximum strain rate is given by $a = 2U/H$. Increasing the gas velocity $U$ or decreasing the distance from the flame tip to the plate $H$ will result in a larger strain rate. Because of the increased strain rate, the boundary layer will be thinner and therefore the heat flux will be increased.

Increasing the distance from the flame tip to the plate $H$ while keeping the gas velocity $U$ constant will have the opposite effect. The strain rate decreases and therefore the heat flux will decrease as well. From a certain distance from the flame tip to the plate, however, the boundary layer will reach its maximum thickness and the maximum strain rate will remain constant. The maximum strain rate is no longer equal to $a = 2U/H$ from this point on. Since the strain rate is independent of the distance $H$ for a ratio of $H/R$ larger than 5/3 [15], the strain rate for large $H/R$ ratios can be defined as $a = 6U/(5R) = 2U/H^*$. The critical distance $H^*$ is defined here as $H^* = 5R/3$. Eq. (1) now can be written as

$$q_0 = \lambda \left.\frac{\mathrm{d}T}{\mathrm{d}x}\right|_0 = \frac{\lambda(T_0 - T_{\mathrm{flame}})}{\int_{-H^*}^{0} \exp\left[-\frac{1}{\alpha}\int_s^0 u\mathrm{d}x\right]\mathrm{d}s}. \tag{4}$$

with

$$H^* = \begin{cases} H & \text{for } H < 5R/3 \\ 5R/3 & \text{for } H \geqslant 5R/3 \end{cases}. \tag{5}$$

Fig. 2 shows the results according to Eqs. (4) and (5) for the heat flux $q$ as a function of the distance from the flame tip to the plate $H$ for a plug flow radius of $R = 1$, 2, 3, 4 and 6 mm (solid lines). For values of the distance $H < 5R/3$, the plug flow radius $R$ has no influence on the heat flux. For values of the distance $H \geqslant 5R/3$, however, the heat flux is no longer dependent on the distance $H$ but becomes dependent on the plug flow radius $R$. Numerical validations for $R = 1$, 2 and 3 mm (asterisks) show very good agreement.

In our previous work [15], we have compared the presented results with the well-known reference work of Sibulkin [16]. Sibulkin solved the boundary layer equations for laminar heat-transfer to a body of revolution near the forward stagnation point. The body of revolution is assumed to be immersed in an infinite, laminar, incompressible, low-speed stream. For the Nusselt number in the stagnation point he found:

$$Nu = 0.763\left(\frac{\beta}{\nu}\right)^{0.5} 2RPr^{0.4}, \tag{6}$$

where the Nusselt number is the ratio of convective to conductive heat transfer $Nu = h2R/\lambda$, with $h$ the heat-transfer coefficient (W/(m$^2$ K)). Also, $\beta = (\partial v/\partial r)_{r=0} = 2U/(\pi R)$ is defined here as the velocity gradient just outside the bound-

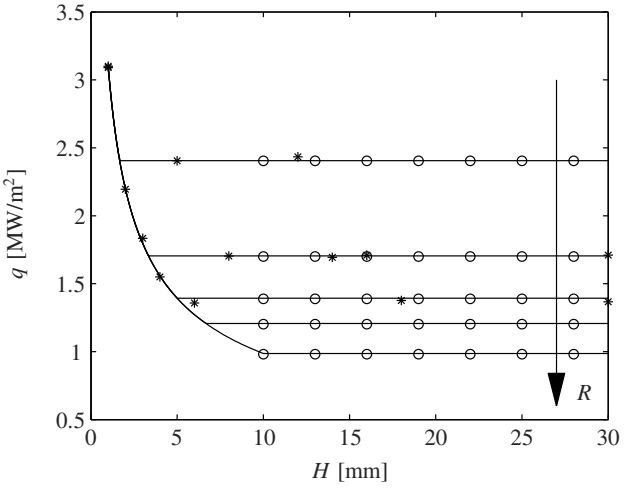


Fig. 2. Convective heat flux as a function of the flame top-to-plate distance $H$ for burnt gas flow tube radii of $R = 1$, 2, 3, 4 and 6 mm. The solid lines represent the analytical solutions, the asterisks the numerical solutions from Fluent and the open circles the results found according to Sibulkin [16].

ary layer [12,18], see Fig. 1. This solution is independent of the flame tip-to-plate spacing and therefore only applicable for larger spacings ($H/R > 8$) [17]. Another characteristic of that solution is that for the limit of a non-viscous situation, an infinite Nusselt number and therefore an infinite heat transfer is predicted.

A comparison with our analytical model is shown in Fig. 2, where the results from Sibulkin are depicted with the circles. The results of the relation according to Sibulkin show very good agreement with the results of our analytical relation for large $H/R$ spacings. The curve in the left part of the figure, representing the convective heat flux for small $H/R$ spacings, is not found by Sibulkin. It can also be noted that with our relation for the convective heat-transfer, a realistic convective heat flux can be calculated for low viscosity flows.

Kleijn [10] investigated the heat-transfer from laminar, round, atmospheric pressure, premixed methane-air flames, impinging perpendicularly on a flat surface. He found the following relation for the heat-transfer to the hot spot for close $H/R$ spacings:

$$q_0 = C\sqrt{\frac{1}{H}}(T_0 - T_{\text{flame}}), \tag{7}$$

where $C$ is a constant ($\text{W}/(\text{m}^{3/2}\,\text{K})$). In this relation, the heat flux is inversely proportional with the square root of the flame tip-to-surface distance $H$. In our derived relation for the heat flux, Eq. (4), we cannot indicate such a dependence at first sight. In a previous work [14], however, we have derived the heat flux of an impinging flame jet for a two-dimensional configuration in a similar manner as shown in this work for the axi-symmetrical configuration. The following heat-transfer relation was derived:

$$q_0 = \lambda(T_0 - T_{\text{flame}})\frac{1}{H}\sqrt{Pe}\cdot\exp[-0.28Pe^{0.40}]. \tag{8}$$

Realizing that $Pe = UH/\alpha$, a similar inversely proportional dependence on the square root of the flame tip-to-surface distance $H$ can be revealed. A significant difference, however, can be pointed out as well. Eq. (7) shows that the heat flux is not a function of the Reynolds number, since $C$ is a constant. Eq. (8) indicates that the heat-transfer actually is a function of the Reynolds number. Since higher gas velocities cause a decrease in the viscous boundary layer thickness at the surface and therefore a higher heat flux from the flame to the target, it is easy to understand that the heat flux should be a function of the Reynolds number.

## 3. Heat–flux distribution

In the previous section we have shown how the heat flux from an oxy-fuel flame to a glass product can be calculated. Therefore, the distance from the flame tip to the plate $H$ and the burnt gas jet radius $R$ together with the burnt gas velocity $U$, burnt gas temperature $T_{\text{flame}}$ and burnt gas properties need to be known. This predicted heat flux, however, is only valid near the hot spot of the product, from $r = 0$ to $r = R$ [15]. Further away from the hot spot a decay of the heat flux takes place. Since this part of the heat flux only has a small influence on the total heat transport from the flame to the product, we will model the heat-transfer numerically and show how this part of the heat flux can be approximated by an exponential function of $r/R$.

Fig. 3 represents the model we used to perform the calculations. Flow and heat-transfer calculations have been performed using the CFD package Fluent for a plug flow of burnt gases with different jet radii $R$ heating a flat quartz plate. In practice, the typical radius of glass tubes is of the order $10^{-2}$ m, while the shell thickness is of the order $10^{-4}$–$10^{-3}$ m. Therefore, the glass product is visualized as a flat plate with thickness $L$. Variations of the distance between the flame tip and the plate $H$ have been considered as well. Since the configuration is axisymmetric, the left boundary of the domain is a symmetry axis. All four boundaries of the plate are walls. At the right part of the domain as well as at the remaining bottom part, the burnt gases flow away through pressure boundaries.

For the numerical calculations, the gas parameters are chosen to be constant with $\rho = \rho_b = 0.083\ \text{kg/m}^3$, $c_p = 2000\ \text{J/(kg K)}$, $\mu = 5.6\cdot 10^{-5}\ \text{kg/(m s)}$ and $\lambda = 0.16\ \text{W/(m K)}$. The values for $c_p$, $\lambda$ and $\mu$ are chosen at a temperature of 1500 K using the transport data documented by Kee and Miller [26] and the thermodynamic data from the GRI-mech 3.0 mechanism. Remie [27] has shown that the heating of the quartz plate with temperature dependent $\lambda$, $\rho$ and $c_p$ is almost the same as the heating with temperature independent parameters, if the temperature independent $\lambda$ is chosen equal to 0.75 times the value at 300 K. Therefore, the parameters of the quartz plate are chosen to be equal to $\rho = 2250\ \text{kg/m}^3$, $c_p = 780\ \text{J/(kg K)}$ and $\lambda = 0.75\cdot 1.4\ \text{W/(m K)}$ [28].

For the first part of the calculation, the temperature of the glass was fixed at a temperature of $T = 300$ K; a steady solution was obtained for the flow field. After the steady solution was obtained, the temperature of the glass was not fixed anymore and the heating of the plate was calculated using an unsteady segregated implicit solver using time steps of $\Delta t = 0.01$ s. This method of working is possible because the time scale of the flow is much smaller than the time scale of the heating of the plate.

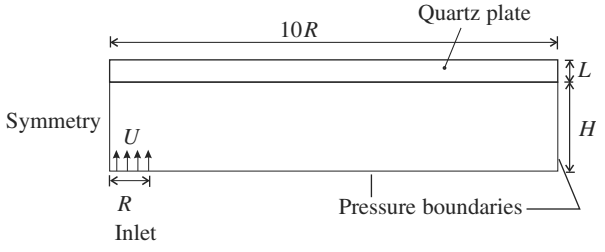


Fig. 3. Schematic of the numerical model used to calculate the heat–flux distribution near the hot side of the plate.

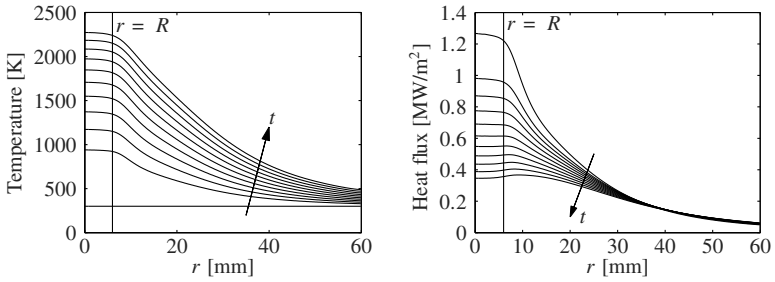


Fig. 4. Temperature $T$ (left) and heat flux $q$ (right) at the hot side of the plate as a function of the radial distance $r$ for $t = 0$–5.0 s, with steps of 0.5 s. The direction of the arrow indicates an increasing value of $t$; $U = 75$ m/s, $T_{\text{flame}} = 3000$ K, $H = 6$ mm, $R = 6$ mm, $L = 1$ mm, $T_0$ $(t = 0) = 300$ K.

Fig. 4 shows the time history of the temperature $T$ (left) and heat flux $q$ (right) at the hot side of the plate as a function of the radial distance $r$ to the symmetry axis. For these calculations a value of $H = 6$ mm for the distance between the inlet and the plate was chosen, while the burnt gas velocity was set to $U = 75$ m/s and the burnt gas temperature to $T_{\text{flame}} = 3000$ K. The burnt gas jet radius was equal to $R = 6$ mm and the thickness of the plate to $L = 1$ mm. Initially, the plate is at a temperature of $T_0 = 300$ K, where the subscript 0 refers to the position at the hot side of the plate. As these figures show, the temperature as well as the heat flux are nearly constant within the hot spot between $r = 0$ and $r = R$ at the different time instants. Outside the hot spot, a decay of the temperature as well as the heat flux can be observed. Moreover, the shape of the temperature curves as well as the heat–flux curves remains approximately the same in time. Consequently, the temperature profiles and heat–flux profiles over the hot side of the plate seem to be close to self-similar.

To check the self-similarity, the numerically calculated heat flux will be made dimensionless by dividing it by the analytically calculated heat flux (at the hot spot) and will be plotted as a function of the dimensionless radial distance $r/R$. The analytical heat flux can be expressed as follows:

$$q = h(T_0 - T_{\text{flame}}), \tag{9}$$

where $h$ [W/(m$^2$ K)] is the analytically calculated convective heat-transfer coefficient to the hot spot and $T_0$ the local temperature at the hot side of the plate, obtained by the numerical calculations. Using Eq. (1), the analytically calculated convective heat-transfer coefficient $h$ will be equal to:

$$h = \frac{\lambda}{\int_{-H}^{0} \exp\left[-\frac{1}{\alpha}\int_{s}^{0} u\mathrm{d}x\right]\mathrm{d}s}. \tag{10}$$

Fig. 5 shows the ratio of the numerical heat flux to the analytical heat flux as a function of the dimensionless radial distance $r/R$. For all times the dimensionless heat–flux profile is almost equal to one in the hot spot, with a small deviation as $r$ becomes equal to $R$. In time, the decrease of the dimensionless heat flux further away from the hot spot remains almost the same. This implies, that the shape of the dimensionless heat flux as function of time is as good as independent of the temperature distribution at the hot side of the plate.

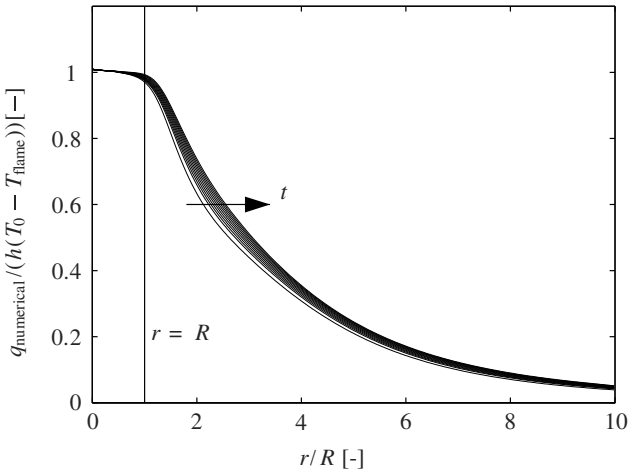


Fig. 5. Ratio of the numerically calculated heat flux and the analytical heat flux at the hot spot as a function of $r/R$ at times $t = 0$–5.0 s, with steps of 0.5 s. The direction of the arrow indicates an increasing value of $t$; $U = 75$ m/s, $T_{\text{flame}} = 3000$ K, $H = 6$ mm, $R = 6$ mm, $L = 1$ mm, $T_0$ $(t = 0) = 300$ K.

To validate this statement also for another initial temperature, Fig. 6 shows the results of the same calculations again, but now the initial temperature distribution at the hot side of the plate was changed to $T_0 = 300 + (1000 - 300)r/0.06$. Plotting the dimensionless heat flux as a function of the dimensionless radial distance to the symmetry axis $r/R$ again indicates the global self-similarity of the heat–flux profiles, as long as the temperature gradient at $t = 0$ s near the hot side of the plate is not too high, see Fig. 7.

Finally, for an initial temperature of $T_0 = 300$ K the same calculations have been performed, but now with different distances between the inlet and the plate $H$ and different burnt gas radii $R$. Calculations have been performed for different combinations of $H = 2$, 3 or 6 mm with $R = 2$, 3 or 6 mm, see Fig. 8 for the results at $t = 0$ s. The results are represented by the dotted lines. All calculations show that the dimensionless heat flux is nearly equal to one within the hot spot. Further away from the hot spot, an 'exponential' decrease can be observed which is more or less the same for all cases. Since the contribution of the heat flux outside the hot spot to the heating of the glass product is less than the contribution of the heat flux inside

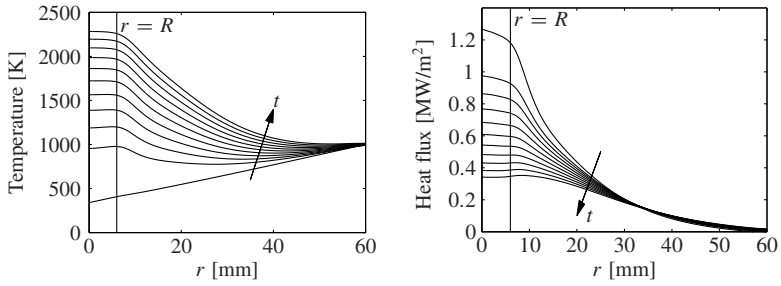


Fig. 6. Temperature $T$ (left) and heat flux $q$ (right) at the hot side of the plate as a function of the radial distance $r$ for $t = 0$–5.0 s, with steps of 0.5 s. The direction of the arrow indicates an increasing value of $t$; $U = 75$ m/s, $T_{\text{flame}} = 3000$ K, $H = 6$ mm, $R = 6$ mm, $L = 1$ mm, $T_0\,(t = 0) = 300 + (1000 - 300)r/0.06$ K.

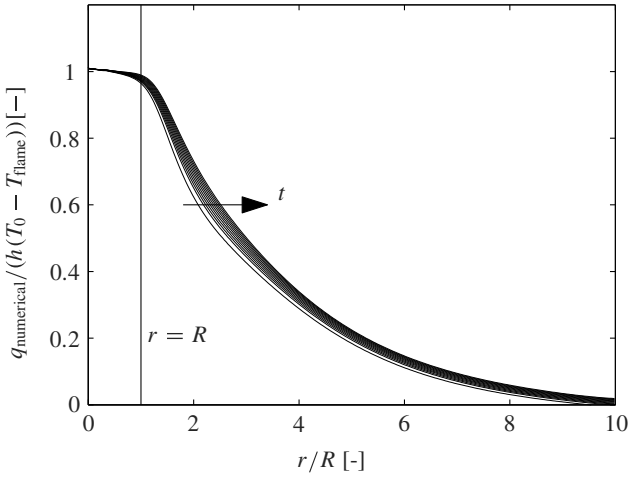


Fig. 7. Ratio of the numerically calculated heat flux and the analytical heat flux at the hot spot as a function of $r/R$ at times $t = 0$–5.0 s, with steps of 0.5 s. The direction of the arrow indicates an increasing value of $t$; $U = 75$ m/s, $T_{\text{flame}} = 3000$ K, $H = 6$ mm, $R = 6$ mm, $L = 1$ mm, $T_0\,(t = 0) = 300 + (1000 - 300)r/0.06$ K.

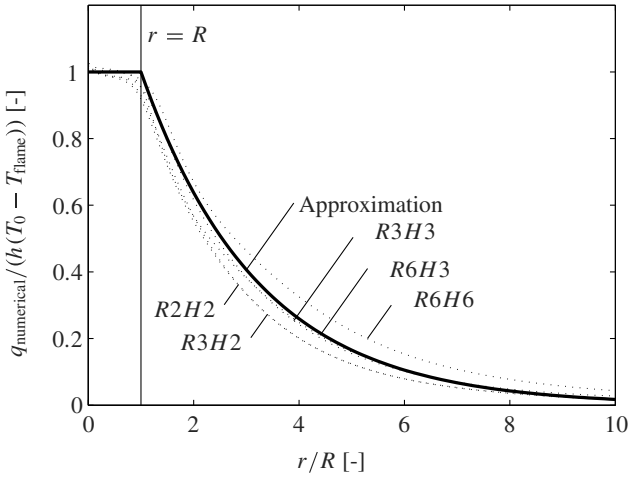


Fig. 8. Ratio of the numerically calculated heat flux and the analytical heat flux at the hot spot as a function of $r/R$ at $t = 0$ s; $U = 75$ m/s, $T_{\text{flame}} = 3000$ K, $L = 1$ mm, $T_0\,(t = 0) = 300$ K; the dotted lines represent the results for the calculations with varying $H$ and $R$, the solid thick line the approximation, defined by Eqs. (11) and (12).

the hot spot, we have chosen to approximate the dimensionless heat flux by an exponential function, instead of performing a full analysis for this region. This approximation is purely made on the basis of numerical computation.

The relation for the convective heat flux from the impinging flame jet to the plate can be divided in a relation applicable at the hot spot from $r = 0$ to $r = R$ and a relation applicable further away from the symmetry axis $r > R$. The convective heat–flux distribution can be expressed as follows (see the thick line in Fig. 8):

$$q = h(T_0 - T_{\text{flame}}) \quad 0 < r/R < 1, \tag{11}$$

$$q = h(T_0 - T_{\text{flame}})\exp[-0.45(r/R - 1)] \quad r/R \geqslant 1. \tag{12}$$

## 4. Experimental validation

In this section some two-dimensional temperature measurements will be presented with which Eq. (12) can be validated. Like for the single-spot temperature measurements [15], the measurement technique is based on phosphor thermometry. A Nd:YAG laser was used to excite the phosphor. The lifetime of the phosphorescence decay and the emission line intensities are temperature sensitive. For the single-spot temperature measurements, the lifetime of the decay of the phosphorescence was extracted, in order to obtain the plate temperature. For the two-dimensional temperature measurements, however, a spectral method was used instead of a temporal method. Now the intensity of two different emission lines is imaged. Since the ratio of these two apparent peak intensities of the phosphor is only dependent on temperature, this technique is suitable for measuring the temperature distribution of the cold site of the quartz plate heated by an impinging flame jet. Spectral profiles of different phosphors are reported by Omrane [29], while a more detailed analysis of the measurement method can be found in refs. [29–32].

Fig. 9 shows a schematic overview of the experimental set-up. For these two-dimensional temperature measurements, the thermographic phosphor YAG:Dy was used. Excitation of the phosphor was conducted using the third harmonic at 355 nm of an Nd:YAG laser with a pulse duration of 8 ns and a repetition rate of 10 Hz. A laser intensity of 130 mJ was used to obtain phosphorescence. The laser light was directed to the top side of the quartz plate. To split the measured image into two identical

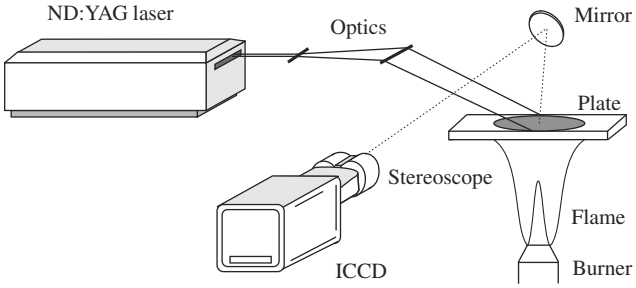


Fig. 9. Schematic overview of the experimental set-up consisting of an Nd:YAG laser, ICCD, stereoscope, optics, mirror and burner.

images, one for each of the emission lines, a stereoscopic device with an interference filter of 458 nm and an interference filter of 493 nm was adapted to the objective of an intensified charge-coupled device (ICCD) camera. For the experiment, a quartz plate with dimensions 100 mm × 100 mm × 5 mm and a burner with nozzle-exit diameter of $d = 1.7$ mm were used. Measurements were performed for a methane-oxygen as well as a hydrogen–oxygen flame with an unburnt gas velocity of 70 m/s and different flame tip-to-plate distances $H$. The premixed gas mixture was supplied to the burner using a mixing panel with mass flow controllers (MFCs), which were set and monitored using an interface to a PC.

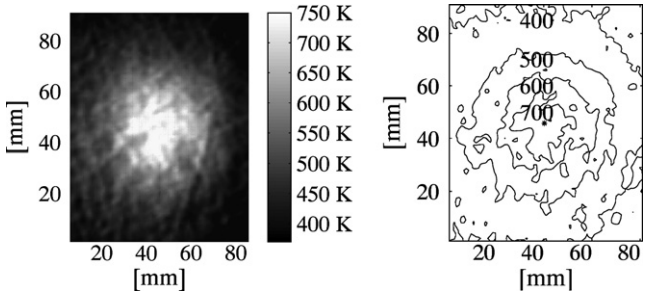


Fig. 10. Temperature distribution of the cold site of the plate after 8 s visualized with a grayscaling (left) and isothermal contours (right); the center of the hot spot is indicated by the asterisk in the right figure. The plate was heated by a hydrogen–oxygen flame; $U = 70$ m/s, $R = 2.4$ mm, and $H = 20$ mm.

Fig. 10 shows a typical result of a temperature distribution measurement of the top side of the plate after $t = 8$ s. The plate was heated by a hydrogen–oxygen flame with $U = 70$ m/s and $H = 20$ mm. After each measurement, the plate was cooled down to approximately 400 K before the next measurement was performed. In the right figure, the center of the hot spot is visualized by the asterisk. Its position was determined as the center of 'mass' of the temperature distribution.

The heating curves of the hot spot at the cold side of the plate were determined using the PDEPE solver of MATLAB [33], in which the one-dimensional instationary conduction equation is solved. Radiative losses were not taken into account, since only the initial part of the heating process is considered. A non-linear least squares fitting procedure was used to compare the numerically obtained heating curves of the hot spot at the cold side of the plate with the experimentally obtained heating curves of the hot spot at the cold side of the plate. For every measurement, a convective heat flux can be determined experimentally as well as analytically. Fig. 11 shows the comparison between the analytically and the experimentally obtained convective heat fluxes for the methane-oxygen flame (left) and the hydrogen–oxygen flame (right). The analytical solutions are represented by the solid lines, the circles represent the experimentally determined heat fluxes. The horizontal error bars are obtained by taking into account the inaccuracy of the manual set flame tip-to-plate distance $H$ (0.2 mm, which is approximately the flame thickness). The vertical error bars are obtained by using a 95% confidence interval ($2\sigma$ error) of the variance of the heat-transfer coefficient $h$. For large flame tip-to-plate distances the convective heat flux is constant, while the convective heat flux at small flame tip-to-plate distances becomes very sensitive for small shifts in distance $H$. It has to be stated that the results are sensitive to measurement errors and input parameters. The purpose of Fig. 11, however, is to show the qualitative behaviour of the heat flux, i.e. to show the distance $H$ from where on the convective heat flux is constant.

Using the results of Fig. 10, a scatter plot of the temperature at the cold side of the plate as a function of the radial

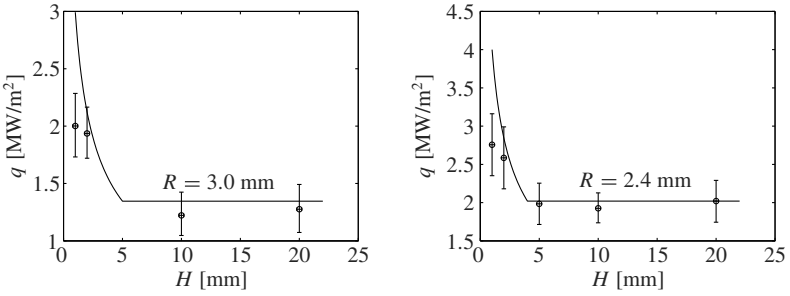


Fig. 11. Convective heat flux $q$ as a function of the flame tip-to-plate distance $H$ for a burnt gas flow tube radius of $R = 3.0$ mm (left) and $R = 2.4$ mm (right). The solid lines represent the analytical solutions, the circles with error bars the measurements with the methane-oxygen flame (flame height $H_{\text{flame}} = 15$ mm) for $R = 3.0$ mm (left) and with the hydrogen–oxygen flame (flame height $H_{\text{flame}} = 5$ mm) for $R = 2.4$ mm (right); $U = 70$ m/s and $H = 1$, 2, 10 and 20 mm (left) and $H = 1$, 2, 5, 10 and 20 mm (right).

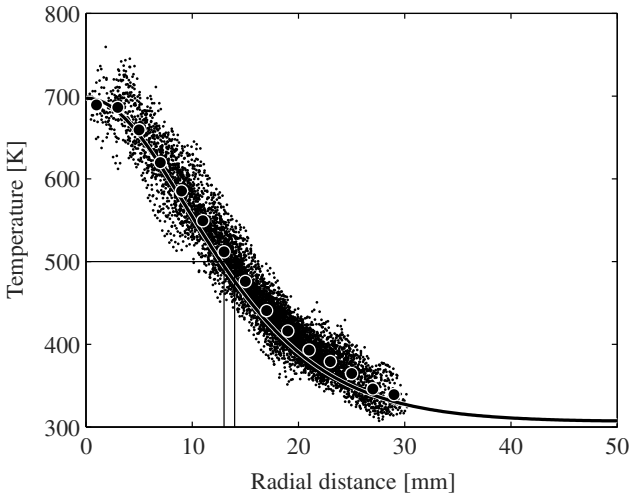


Fig. 12. Typical temperature distribution of the cold side of the quartz plat as a function of the radial distance to the center of the hot spot at $t = 8$ s. The plate was heated by a methane-oxygen flame, with $U = 70$ m/s and $H = 10$ mm. The small dots represent the measurement results, the big dots the averaged measurement results and the solid line the numerically obtained results. The thin solid lines show the difference in the numerically and experimentally obtained half maximum – half width values.

Table 1
Values of the half maximum – half width value differences between the experiments and the numerical calculations

| | $H = 1$ mm | $H = 2$ mm | $H = 5$ mm | $H = 10$ mm | $H = 20$ mm |
|---|---|---|---|---|---|
| $CH_4$–$O_2$ | 1.0 mm | 2.0 mm | – | 1.5 mm | 2.0 mm |
| $H_2$–$O_2$ | 4.0 mm | 1.0 mm | 1.0 mm | 0.5 mm | 2.0 mm |

distance to the center of the hot spot can be obtained. Such a scatter plot is shown in Fig. 12. A methane-oxygen flame was used to heat the plate, with $U = 70$ m/s and $H = 10$ mm. The big dots represent the averaged measurement results. To obtain such a temperature distribution curve numerically, the same calculations were performed as explained in the previous section. A plate with thickness $L = 5$ mm was heated using the heat–flux boundary Eqs. (11) and (12). For the velocity $U$ and the flame tip-to-plate distance $H$, the same values were used as in the experimental configuration. In Fig. 12, the numerical result is represented by the solid line.

To validate the heat–flux distribution relation given by Eq. (12), Fig. 12 shows the half maximum – half width values of the numerically and experimentally obtained temperature distribution. For this situation, the difference is only 1.5 mm and therefore Eq. (12) seems to hold. Table 1 shows the results of all the measurements. Only for the measurements with the hydrogen–oxygen flame with $H = 1$ mm, a considerable difference was observed.

## 5. Conclusions

In the glass heating process, it is important to know what the temperature distribution inside the product is, considering internal thermal stresses. Therefore, the heat–flux distribution of an impinging flame jet to a glass product is essential. In a previous work [15] a relation was already presented for the convective heat flux of an impinging flame jet to the hot spot of the product. In this paper an additional part of the convective heat–flux relation is studied at larger radial distances from the hot spot. At the edge of the hot spot at $r = R$, the two heat–flux relations are linked to each other.

Experimental validations have been performed for the analytical convective heat–flux relations. For that purpose, phosphor thermometry techniques have been applied. For the validation of the convective heat–flux relation applicable at the hot spot, single-point temperature measurements have been carried out and presented in a previous work [15]. In this work, two-dimensional temperature measurements have been carried out as well. The results clearly show that the heat flux is constant for large flame tip-to-plate distances and increases rapidly for shorter distances, which is in agreement with the analytical heat–flux relations. Moreover, the temperature measurements show good agreement with the heat–flux relations applicable at radial distances away from the hot spot.

## Acknowledgement

The financial support by Philips Lighting B.V. is gratefully acknowledged.

## References

[1] R. Viskanta, Heat transfer to impinging isothermal gas and flame jets, Exp. Therm. Fluid Sci. 6 (1993) 111–134.
[2] R. Viskanta, Convective and radiative flame jet impingement heat transfer, Int. J. Transport Phenom. 1 (1997) 1–15.
[3] C.E. Baukal, B. Gebhart, A review of flame impingement heat transfer studies. Part 1. Experimental conditions, Combus. Sci. Technol. 104 (1995) 339–357.
[4] C.E. Baukal, B. Gebhart, A review of flame impingement heat transfer studies. Part 2. Measurements, Combus. Sci. Technol. 104 (1995) 359–385.
[5] L.L. Dong, C.W. Leung, C.S. Cheung, Heat transfer of a row of three butane/air flame jets impinging on a flat plate, Int. J. Heat Mass Transfer 46 (2003) 113–125.
[6] L.L. Dong, C.W. Leung, C.S. Cheung, Heat transfer and wall pressure characteristics of a twin premixed butane/air flame jets, Int. J. Heat Mass Transfer 47 (2004) 489–500.
[7] L.C. Kwok, C.W. Leung, C.S. Cheung, Heat transfer characteristics of slot and round premixed impinging flame jets, Exp. Heat Transfer 16 (2003) 111–137.
[8] L.C. Kwok, C.W. Leung, C.S. Cheung, Heat transfer characteristics of an array of impinging pre-mixed slot flame jets, Int. J. Heat Mass Transfer 48 (2005) 1727–1738.
[9] Z. Zhao, T.T. Wong, C.W. Leung, Impinging premixed butane/air circular laminar flame jet – influence of impingement plate on heat transfer characteristics, Int. J. Heat Mass Transfer 47 (2004) 5021–5031.
[10] C.R. Kleijn, Heat transfer from laminar impinging methane/air flames, Computational Technologies for Fluid/Thermal/Structural/Chemical Systems With Industrial Applications, vol. 1, ASME, 2001, pp. 259–269.
[11] S. Chander, A. Ray, Heat transfer characteristics of three interacting flame jets impinging on flat surface, Int. J. Heat Mass Transfer 50 (2007) 640–653.

[12] T.H. van der Meer, Heat transfer from impinging flame jets, PhD Thesis, Delft University of Technology, 1987.
[13] C.E. Baukal, B. Gebhart, Surface condition effects on flame impingement heat transfer, Exp. Therm. Fluid Sci. 15 (1997) 323–335.
[14] M.J. Remie, M.F.G. Cremers, K.R.A.M. Schreel, L.P.H. de Goey, Analysis of the heat transfer of an impinging laminar flame jet, Int. J. Heat Mass Transfer 50 (2007) 2816–2827.
[15] M.J. Remie, G. Särner, M.F.G. Cremers, A. Omrane, K.R.A.M. Schreel, M. Aldén, L.P.H. de Goey, Extended heat transfer relation for an impinging laminar flame jet to a flat plate, Int. J. Heat Mass Transfer, in press.
[16] M. Sibulkin, Heat transfer near the stagnation point of a body of revolution, J. Aeronaut. Sci. 19 (1952) 570–571.
[17] P.S. Shadlesky, Stagnation point heat transfer for jet impingement to a plane surface, AIAA J. 21 (8) (1983) 1214–1215.
[18] W.M. Kays, Convective Heat and Mass Transfer, McGraw-Hill, New York, 1966.
[19] V. Kottke, H. Blenke, K.G. Schmidt, Messung und Berechnung des ortlichen und mittleren Stoffübergangs an stumpf angestromten Kreisscheiben bei unterschiedlicher Turbulenz, Wärme und Stoffübertragung 10 (1977) 89–105.
[20] C.E. Baukal Jr., Heat Transfer in Industrial Combustion, CRC Press LLC, Boca Raton, 2000.
[21] J.K. Kilham, M.R.I. Purvis, Heat transfer from normally impinging flames, Combus. Sci. Technol. 18 (1978) 81–90.
[22] M.F.G. Cremers, M.J. Remie, K.R.A.M. Schreel, L.P.H. de Goey, Heat transfer mechanisms of laminar flames of hydrogen+oxygen, Combust Flame 139 (2004) 39–51.
[23] M.F.G. Cremers, M.J. Remie, K.R.A.M. Schreel, L.P.H. de Goey, Thermochemical heat release of laminar stagnation flames of fuel and oxygen, Combust Flame, under review (2007).
[24] M.J. Remie, M.F.G. Cremers, K.R.A.M. Schreel, L.P.H. de Goey, Flame jet properties of Bunsen-type flames, Combust Flame 147 (2006), 163:170.
[25] ⟨http://www.fluent.com⟩.
[26] R.J. Kee, J.A. Miller, A structured approach to the computational modeling of chemical kinetics and molecular transport in flowing systems, Springer Series Chem. Phys. 47 (1986) 196.
[27] M.J. Remie, Heat transfer from flames to a quartz plate, Msc. Thesis, Eindhoven University of Technology, Rep. Nr. WVT 2002.01, 2002.
[28] A. Bejan, Heat Transfer, John Wiley & Sons, Inc., 1993, ISBN 0-471-50290-1.
[29] Alaa Omrane, Thermometry using laser-induced emission from thermographic phosphors: development and applications in combustion, Ph.D. Thesis, Lund Institute of Technology, 2005.
[30] S.W. Allison, G.T. Gillies, Remote thermometry with thermographic phosphors: instrumentation and applications, Rev. Sci. Instrumen. 68 (7) (1997) 1–36.
[31] A. Omrane, G. Juhlin, M. Aldén, G. Josefsson, J. Engtström, T. Benham, Demonstration of two-dimensional temperature characterization of valves and transparent piston in a GDI optical engine, SAE, 2004-01-0609.
[32] H. Seyfried, G. Särner, A. Omrane, M. Richter, H. Schmidt, M. Aldén, Optical diagnostics for characterization of a full-size fighter-jet afterburner, in: Proceedings of ASME GT2005, GT2005-69058.
[33] ⟨http://www.mathworks.com/access/helpdesk/help/techdoc/ref/pdepe.html⟩.